Nanoscale Horizons

ROYAL SOCIETY OF CHEMISTRY

COMMUNICATION

View Article Online
View Journal | View Issue

Check for updates

Cite this: *Nanoscale Horiz.*, 2025, **10**, 3405

Received 12th April 2025,
Accepted 2nd September 2025

DOI: 10.1039/d5nh00231a

rsc.li/nanoscale-horizons

Quantitative 2D fitting of fluorescence-excitation maps: excitation lineshape of single-wall carbon nanotubes

Sofie Cambré, †‡ Wouter Van Werveke, ‡ Miguel De Clercq, ‡ Maksiem Erkens, Miles Martinati and Wim Wenseleers *

Two-dimensional (2D) fluorescence-excitation (PLE) spectroscopy offers a powerful way to analyse samples of semiconducting single-wall carbon nanotubes (SWCNTs). The one-to-one correspondence between the SWCNT chiral structure and its optically excited states allows for the identification of individual species based on peaks in 2D PLE data. Changes in the position, width and other features of the lineshape associated with a given peak reveal a plethora of information about the associated SWCNT chirality and *e.g.* its interactions with the environment. Consistent and physically relevant quantification of that information requires accurate fitting of the 2D data, which has long been hindered by the fact that a sufficiently accurate functional form for the excitation profile of SWCNTs was not known. Here we present a highly accurate analytical empirical model for the excitation lineshape and combine it with one for the emission lineshape in a 2D fitting model that produces accurate fits of 2D PLE maps for any SWCNT sample and allows straightforward extraction of lineshape features, including peak positions, linewidths and intensities as well as other relevant physical quantities such as phonon sidebands in the emission and excitation spectra.

New concepts

We introduce a novel, quantitatively accurate model for fitting 2D photoluminescence-excitation (PLE) spectra of single-wall carbon nanotubes (SWCNTs), resolving a long-standing challenge in nanotube spectroscopy. Unlike previous approaches, which relied on simplified or incomplete descriptions of the excitation profile and were primarily limited to estimating chirality abundances, our model explicitly accounts for both excitonic and band-to-band contributions, yielding an unprecedentedly accurate representation of the excitation lineshape. This allows for precise extraction of fundamental spectral parameters—peak positions, linewidths, intensities, and phonon sidebands—enabling a far more complete and generalizable characterization of SWCNTs. Crucially, our model captures environmental effects such as nanotube filling, solvent interactions, and surfactant wrapping, which were previously challenging to quantify. This capability advances the use of PLE spectroscopy beyond chirality identification, facilitating a deeper understanding of SWCNT optical properties across different conditions. By integrating this model into a user-friendly software tool, we provide the nanoscience community with a robust and accessible method for high-precision spectral analysis. This breakthrough significantly enhances the potential of SWCNT research towards optoelectronic, sensing, and quantum applications by enabling detailed and reliable characterization at an unprecedented level.

Introduction

The electronic and optical properties of single-wall carbon nanotubes (SWCNTs) depend critically on their structure, uniquely identified by the chiral indices (n, m), which determine the diameter and chiral angle of a given SWCNT.[1] The first structure-specific calculations of these optical properties were done by Kataura *et al.* who used a zone-folding approach to derive a relation between the optical transition energies (E_{11}, E_{22}) of SWCNTs and their diameter and chiral structure.[2] Subsequently, Bachilo *et al.* empirically modified the Kataura relations through PLE spectroscopy measurements, enabling effective identification of SWCNTs.[3] Since bulk SWCNT samples typically contain a wide range of diameters and chiral structures after synthesis, identifying every chiral species in a mixed chirality sample is highly valuable both for academic research and for the integration of SWCNTs in future applications, particularly those that exploit the structure-dependent properties of the SWCNTs.

A powerful spectroscopic technique that allows to take full advantage of the one-to-one correspondence between (E_{11}, E_{22}) and (n, m) is photoluminescence-excitation (PLE) spectroscopy. In this technique a sample is optically excited with a varying excitation energy, *e.g.* exciting SWCNTs at the E_{22} transition, and the subsequent emission at E_{11} is measured. The resulting two-dimensional (2D) intensity map contains a peak for every

Nanostructured and Organic Optical and Electronic Materials, Physics Department, University of Antwerp, Belgium. E-mail: Wim.Wenseleers@uantwerp.be

† Current address: Theory and Spectroscopy of Molecules and Materials, Physics Department, University of Antwerp, Belgium.

‡ These authors contributed equally to this work.

fluorescent SWCNT chirality in the investigated sample. Since metallic nanotubes relax nonradiatively, PLE spectroscopy can measure only semiconducting (SC) nanotubes. Nonetheless, it is a potent and widely used technique for identifying individual SC SWCNT species in a given sample and measuring or comparing their intensities, which can be related to their abundances if the chirality- and environment-dependent photoluminescence quantum efficiency is known or can be reliably estimated. Thus PLE spectroscopy can be used for example to quickly and quantitatively establish the chirality distribution of the semiconducting SWCNTs present in a mixed-chirality sample, *e.g.* essential for assessing the purity of sorted SWCNT samples.[4–8] Furthermore, PLE spectroscopy provides quantitative information about variations in the optical properties of SWCNTs, such as changes in the transition energy and excitation lifetime as a result of altered interactions with different external (*e.g.* surfactant solubilisation, polymer wrapping, functionalisation)[9–11] or internal (filling with various molecules) environments.[12–16] Additionally, phonons can be explored through phonon-assisted excitation and emission in a SWCNT, which manifest as sidebands of the main peak in PLE maps.[17–21] PLE spectroscopy is also widely used to investigate and quantify the defect-state photophysics in covalently functionalised SWCNTs, represented by lower-energy emission peaks in the PLE spectrum.[22,23]

In order to both qualitatively and quantitatively describe all these phenomena, an accurate and tractable model is required. However this has been a challenge within the nanotube community, since an accurate model function for the excitation lineshape for SWCNTs has not been derived, yet. In particular, the lineshape contains a long tail which is unexplained by purely excitonic optical transitions and has to date not been satisfactorily dealt with in existing fitting procedures. This tail is attributed to band-to-band transitions, and has been investigated before by Vialla *et al.*[24] Other studies have focused on the excitonic contributions to the excitation profile, for instance identifying phonon sidebands,[25] or extracting linewidths as a measure for intersubband decay.[26] In these studies, a full 2D fitting of the PLE maps is generally not attempted. Instead, one approach has been to integrate the 2D PLE map over a range of excitation wavelengths, chosen wide enough to contain as much of the peaks of interest as possible but sufficiently narrow to avoid overlapping contributions from other peaks.[13] The integrated emission spectrum for the peaks within that range can then be fitted. Similarly an integration over a range of emission wavelengths could be performed and the integrated excitation spectrum subjected to a fitting procedure. However, without a model for the excitation lineshape, an accurate fit is impossible – let alone a physically meaningful one.

Another way PLE maps have been fitted is by performing a fit of the emission spectra at each excitation wavelength.[27] The idea here is that for every peak in the 2D map, so every nanotube chirality, a Voigt curve is fitted in the emission spectra, with shared linewidth and peak position across all excitation wavelengths. This results in an emission lineshape for each chirality, a linear combination of which is fitted to the emission spectrum at every excitation wavelength in the PLE map. This nicely circumvents the difficulties with the unknown excitation lineshape, which can be approximated in this method by combining the fitted Voigt peaks for each excitation wavelength. This also allows to *e.g.* determine the relative intensity of the energy transfer of porphyrins, adsorbed on the outer SWCNT walls, with respect to the E_{22} excitation of the corresponding SWCNT, which was previously exploited to obtain absorption cross-sections as a function of SWCNT chirality.[27] In ref. 24, a similar approach of 1D fitting of a series of emission spectra as a function of excitation wavelength was used to extract detailed excitation spectra, allowing for investigating the band-to-band contribution in between excitonic resonances, and drawing important conclusions about the universality of this nonresonant contribution across different chiralities. In that work, it is concluded that this band-to-band contribution is essentially constant. However, we found that a constant ''background'' is insufficiently accurate to enable a full 2D fit of the PLE maps, as we observe a significant downward slope with increasing energy, and a significantly higher intensity above than below the E_{22} excitonic resonance (trends that are actually also observable in the data of ref. 24). Therefore we derived a more accurate model function for this band-to-band excitation (see below).

A third method, described in ref. 28, uses comparison with simulated spectra. In this case, a 2D model is used to fit PLE maps from reference samples and the optimised model parameters are stored in a database. Then, these parameters are assumed to be the same for different samples and are thus used to construct the full PLE mpas from just a few excitation wavelengths. The model used in this method consists of a 2D fitting function for each SWCNT chirality, defined as the product of lineshape functions for emission and excitation, with an amplitude pre-factor so that the sum of all these individual 2D functions together can reproduce a bulk sample PLE map. The emission lineshape function contains a single (Voigt) peak, without phonon sidebands. The excitation profile is modelled as a weighted sum of a main E_{22} peak, three phonon sidebands, a constant background and a sideband of the E_{11} peak, where the main peak has a fixed weight of 1 and the E_{11} sideband has its position and width fixed with respect to those of the E_{11} peak. Using this model, reference spectra containing $\sim$55 different SWCNT chiralities were fitted in advance and the optimised parameters stored. Analysing a new sample is then done by measuring emission spectra at only a few excitation wavelengths and comparing these to simulated emission spectra based on the database parameter values. Optimisation is done at the level of the individual amplitudes of the chiralities only. This makes for a very fast fitting process and could therefore be quite useful for routine characterisation of nanotube samples that are consistent with those in the database. However, it is impossible in this scheme to properly deal with peaks that are shifted or broadened as a consequence of environmental changes with respect to those reference samples, such as different surfactants, solvents, *etc.*[10,12–16]

In this context, it is also worth noting that in contrast to 2D PLE maps, the fitting of absorption spectra of SWCNTs is much more mature, and a comprehensive fitting procedure has been published by Pfohl *et al.*[29] Being one-dimensional data, absorption spectra are less demanding in terms of the model to be used for fitting the broad nonresonant "background" (which, in the case of absorption spectra, unlike PLE, also contains major contributions from scattering and impurities): Pfohl *et al.* show that three different types of empirical background subtraction functions yield comparable results. In contrast, for 2D fitting of PLE maps, all of these empirical backgrounds are insufficiently accurate and/or introduce too many parameters. As 2D PLE maps provide much more detailed information than absorption spectra, the combination of both can be particularly powerful: our approach to the analysis of 2D PLE maps can provide very useful information on the chiralities present and their peak positions and linewidths, which can in turn be used as input to the fitting model of Pfohl *et al.* to fit the absorption spectrum of the same sample, allowing to fix many parameters and obtain even more robust fits.

In this paper, we present an accurate empirical model for the excitation lineshape which, in addition to the main excitonic transitions, assumes band-to-band contributions. Combined with a model for the emission lineshape, this allows for straightforward fitting of any 2D PLE map of a SWCNT sample. Our model has been tested on an extensive collection of samples with widely varying characteristics, going from empty (end-capped) SWCNTs over water-filled ones to nanotubes filled with a wide variety of solvents and dye molecules.[8,14–16,30] Moreover, samples containing anywhere between just a single chiral species and more than 20 chiral species, with diameters from the very thinnest (0.54 nm) up to the largest emitting nanotubes, were investigated.[6,31,32] Finally, the model also allows to accurately reproduce PLE maps of nanotubes in different environments such as in aqueous surfactant solutions or solubilised CNTs through polymer wrapping in toluene solutions, and even for fitting the PLE spectra of the outer SWCNTs of double-wall CNTs.[33]

A good and accurate fit can be obtained for all these samples using this model, strongly suggesting there is physical significance to the assertion that purely excitonic optical transitions in SWCNTs may not paint the full picture. Aside from this important empirical insight, our model provides a straightforward fitting procedure with a limited number of fitting parameters. Importantly, we have developed a Graphical User Interface (GUI) for our code, PLEfit2D, which greatly facilitates the fitting process even for inexperienced users and includes highly useful tools for analysis and visualisation of the fit both during and after the fitting process. PLEfit2D is being distributed under a non-commercial use license at **https://plefit2d.uantwerpen.be**.

Model description

Fitting model

Broadly, our fitting model consists of two layers of complexity: (i) a two-dimensional (2D) function describing the PLE spectrum corresponding to an individual chiral species, and (ii) a linear combination of these individual contributions to make up the full 2D PLE map of a given sample. Hence the model can be written in terms of the emission and excitation energies E_{em} and E_{ex} as

$$\mathbb{F}(E_{\mathrm{em}}, E_{\mathrm{ex}}) = \sum_{i=1}^{N} A_i F_i(E_{\mathrm{em}}, E_{\mathrm{ex}}), \tag{1}$$

where N is the number of distinct chiral species (n, m) in the sample, the index $i \equiv (n, m)$ enumerates these species and each of the 2D functions F_i corresponds to one such chiral species, given by a separable product function:

$$F_i(E_{\mathrm{em}}, E_{\mathrm{ex}}) = M_i(E_{\mathrm{em}}) \times X_i(E_{\mathrm{ex}}). \tag{2}$$

The functions $M_i(E_{\mathrm{em}})$ and $X_i(E_{\mathrm{ex}})$ used to model the emission and excitation lineshapes, respectively, are detailed below.

The fitting happens (simultaneously) on the two aforementioned levels: a non-linear least-squares algorithm is used to optimise the fit of the individual peak shapes and positions described by the functions F_i, while the peak intensities (amplitude) A_i are fitted *via* a simple linear regression scheme. This analytical procedure ensures robustness of the amplitude fitting, as opposed to an iterative convergence algorithm.

Additionally, basis functions that correspond to a constant or bilinear background can also be included in the model, adding N_b terms to the sum in (1), with N_b the number of background basis functions included. Their amplitudes are determined in the same way as those of the chirality-dependent basis functions, such that this does not add any iteratively determined parameters to the fit. (More details can be found in the SI.) In the following, we will drop the index i for simplicity and consider the model for a single SWCNT chirality, unless otherwise specified.

Emission lineshape $M(E_{\mathrm{em}})$

The emission spectrum consists of a main peak, due to radiative recombination from the lowest bright exciton state to the electronic groundstate, and sidebands which find their origins in phonon-assisted emission. We include two phonon modes that can give rise to this type of emission. The so-called K-momentum dark exciton couples to the D-band phonon, which allows it to be scattered into a bright exciton state by emission of such a phonon, giving rise to the observed sideband in emission.[20,21,34] The radial breathing mode (RBM) phonon has previously been found to produce a sideband close to the main exciton peak and is thus responsible for the asymmetric emission lineshape of individual SWCNTs.[13,18]

Our model for the emission lineshape $M(E_{\mathrm{em}})$ assumes a Voigt profile for the main exciton peak, which is a convolution of a Lorentzian lineshape and a Gaussian lineshape, defined as:

$$\begin{aligned} V_{11}(E) &:= V(E; E_{11}, \sigma_{11}, \gamma_{11}) \\ &= \int_{-\infty}^{\infty} G(E'; E_{11}, \sigma_{11}) L(E - E'; 0, \gamma_{11}) \mathrm{d}E' \end{aligned} \tag{3}$$

with

$$G(E;E_0,\sigma)=\frac{1}{\sigma\sqrt{2\pi}}\exp\left[-\frac{(E-E_0)^2}{2\sigma^2}\right] \quad (4)$$

$$L(E;E_0,\gamma)=\frac{1}{\pi}\frac{\gamma}{(E-E_0)^2+\gamma^2}. \quad (5)$$

This peak is fully determined by its central position E_{11} and the linewidth parameters σ and γ of the Gaussian and Lorentzian, respectively. These parameters are related to the full-widths-at-half-maximum (FWHMs, ϕ) of the respective curves they characterise as $\phi_G = 2\sigma\sqrt{2\ln 2}$ and $\phi_L = 2\gamma$. The peak width can alternatively be described by the actual FWHM of the Voigt profile ϕ_V in combination with a shape parameter $\eta := \phi_L/\phi_V$ quantifying the ratio of the Lorentzian and Gaussian contributions. A highly accurate approximation (to $\sim$0.02% at most over the range from pure Gaussian to pure Lorentzian) for the relation between ϕ_V and (ϕ_L, ϕ_G) is given by ref. 35.

$$\phi_V = 0.5346\phi_L + \sqrt{0.216598\phi_L^2 + \phi_G^2}. \quad (6)$$

We favour this description over one in terms of the strongly covariate individual Lorentzian and Gaussian linewidths, since it contains all of the joint variability in the shape parameter η. Additionally, the uncertainty it yields on the overall linewidth is more useful to evaluate the goodness of a fit than those on the individual ϕ_L and ϕ_G. For N chiral species in a sample this leads to $3N$ fitting parameters: E_{11}, ϕ_{11} and η_{11} for each chiral species. We leave out the index V here for simplicity of notation. In our GUI it is possible to manually set η to either 0 or 1, corresponding to resp. a purely Gaussian or a purely Lorentzian lineshape in appropriate situations, reducing the number of fit parameters per chirality to 2.

To improve the computational speed of our model, we make use of a C++ implementation of the Faddeeva function $w(z)$ by Steven G. Johnson at MIT.[36] This code uses a combination of algorithms for the Faddeeva function, providing fast and reliable evaluations of the Voigt function, which is connected to it *via*

$$V(E;E_0,\sigma,\gamma)=\frac{1}{\sigma\sqrt{2\pi}}\mathrm{Re}\left[w\left(\frac{E-E_0+i\gamma}{\sigma\sqrt{2}}\right)\right]. \quad (7)$$

Both the D-band sideband of the K-momentum dark exciton and the RBM phonon sidebands (PSBs), like the main exciton peak, are modelled as Voigtians:

$$V_{K,11}(E) := V(E;E_{K,11},\sigma_{11},\gamma_{11}) \quad (8)$$

$$V_{RBM,11}(E) := V(E;E_{RBM,11},\sigma_{11},\gamma_{11}). \quad (9)$$

Since the exact linewidths of these PSBs are hard to discern, we approximate them by the linewidth of the main E_{11} exciton peak. As a result, the only unknown parameters introduced by including them are the positions $E_{K,11}$ and $E_{RBM,11}$ and their relative amplitudes (*cfr.* eqn (15)). In reality, the position of the *K*-momentum phonon-assisted emission peak relative to the main exciton peak position depends on chiral structure, since the energy gap between the dark *K*-momentum exciton involved and the bright exciton is chirality-dependent.[37] However, the variation is relatively small and therefore we can make the good approximation of adopting a single value for all SWCNT species, which we denote $E_{K,11} \equiv E^{em}_{K,11}$. The superscript "em" indicates the lower-energy PSB, since this is the relevant sideband in emission.

The higher-energy PSB will be important in excitation (see also the discussion at the end of the Excitation lineshape section below) and since this PSB is much more frequently observed than the one in emission, we can eliminate $E^{em}_{K,11}$ as a fit parameter by making use of the fact that they are separated by twice the D-band phonon energy:

$$E^{em}_{K,11} = E^{ex}_{K,11} - 2\hbar\omega_D. \quad (10)$$

Here ω_D = 167.4 meV is the energy of the D-band phonon (frequency ω_D = 1350 cm^{-1}) and $E^{ex}_{K,11}$ corresponds to the higher-energy PSB of the E_{11} transition. Since the PSB observed in excitation is actually $E^{ex}_{K,22}$, we make the additional assumption that

$$E^{ex}_{K,11} - E_{11} = E^{ex}_{K,22} - E_{22}, \quad (11)$$

allowing us to rewrite eqn (10) as follows:

$$E^{em}_{K,11} = E_{11} + E^{ex}_{K,22} - E_{22} - 2\hbar\omega_D. \quad (12)$$

Here E_{22} and $E^{ex}_{K,22}$ are the main exciton peak position and K-momentum PSB in the excitation profile as defined in the Excitation lineshape section below. Both are fitted in our model which means $E^{em}_{K,11}$ is not an additional fitting parameter but can instead be calculated from the relation in eqn (12).

Lastly, the position of the RBM phonon sideband $E_{RBM,11}$ is not fitted but instead determined *via* the formula first analytically derived by Mahan,[38] then empirically adjusted and quantified by Bachilo *et al.*[3] and later fine-tuned within our group:[39]

$$E_{RBM} = \frac{27.50\ \text{meV nm}}{d} + 1.39\ \text{meV}, \quad (13)$$

where d is the diameter of the nanotube species giving rise to the peak to be fitted. It is difficult to quickly and accurately determine this diameter automatically from a PLE map. However, Bachilo *et al.* derived empirical relations between the pairs ($\tilde{\nu}_{11}$, $\tilde{\nu}_{22}$) and (d, α), where α is the chiral angle of the SWCNT, which allow for the prediction of the peak position for any given nanotube. These empirical relations can be inverted to obtain (d, α) from ($E_{11,22}$) and are of the following form:

$$\tilde{\nu}_{jj} = \frac{10^7\ \text{cm}^{-1}}{B^j_1 + B^j_2 d} + \frac{A^j_\mu \cos(3\alpha)}{d^2}\text{cm}^{-1}. \quad (14)$$

Here j = 1, 2 corresponds to the first and second optical transitions respectively, d is the SWCNT diameter in nm, B^j_1 and B^j_2 are parameters which differ for the two optical transitions j and A^j_μ is a parameter depending on both the optical transitions j and the modulus of the SWCNTs (*i.e.* $\mu := (n-m) \bmod 3 = 1, 2$). A variety of values for these parameters has been published before since, similar to the optical transition frequencies themselves, they also depend on the inner and

outer nanotube environment. An overview of the parameters for different internal environments can be obtained in the SI of ref. 16.

By inverting these relations (with the parameters for empty solubilised SWCNTs, see the SI) we obtain diameters which are not physically accurate for a general sample, since the parameters in eqn (14) would have different values for different samples. However, they do act as effective diameters which give accurate predictions of the RBM peak position. Moreover, since these effective diameters still scale appropriately among different nanotube chiralities, we can nevertheless use them to factor out the power-law diameter dependence of the phonon sideband intensities.[40] In particular, we take the amplitude of each peak in the emission lineshape relative to the main exciton contribution, with a factor of d^β modelling this power-law dependence. The exponent β is fitted as a universal parameter, where we make the approximation that it is the same for both phonon modes. Thus the full emission fitting model is given by

$$M(E_{\mathrm{em}}) = V_{11}(E_{\mathrm{em}}) + d^\beta A_{\mathrm{K},11} V_{\mathrm{K},11}(E_{\mathrm{em}}) + d^\beta A_{\mathrm{RBM},11} V_{\mathrm{RBM},11}(E_{\mathrm{em}}) \tag{15}$$

where the phonon sidebands are optional and $E^{\mathrm{em}}_{\mathrm{K},11}$ and $E_{\mathrm{RBM},11}$ are determined using eqn (12) and (13), respectively. There are $3N$ fit parameters in the emission model, namely E^i_{11}, ϕ^i_{11} and η^i_{11}, for each chirality $i \equiv (n, m)$. The optional PSBs add 3 more: the two amplitudes $A_{\mathrm{K},11}$ and $A_{\mathrm{RBM},11}$ and the exponent β in the power-law dependence of the PSB intensity on SWCNT diameter. Fig. 1 contains a PLE map from a sample mainly containing the (6, 5) chiral species in panel (a) and also clearly shows the three constituent components of the emission lineshape in panel (c).

Excitation lineshape $X(E_{\mathrm{ex}})$

Initial descriptions of optical transitions in SWCNTs assumed independent electrons, *i.e.* band-to-band (BTB) transitions between the van Hove singularities.[3,41] Later investigations, however, revealed a strongly bound exciton picture.[42,43] Although it is now generally accepted that the optical excitations in SWCNTs are indeed dominated by excitons, PLE maps exhibit prominent long tails which cannot be explained by purely excitonic excitation and may be attributed to BTB transitions. Fig. 1 shows a PLE map from a sorted sample of (6,5) SWCNTs,[4] where the long tails from BTB excitation can be clearly observed. As can also be seen, the main peak at E_{22} additionally exhibits a sideband due to phonon-assisted excitation related to the D-band phonon interacting with the dark K-momentum exciton, analogous to the emission spectrum.[17] Finally, the peaks associated with excitation in the E_{11} transition fall outside of the range of typical PLE maps, but their long BTB tails still influence the excitation spectrum and have to, therefore, be accounted for.

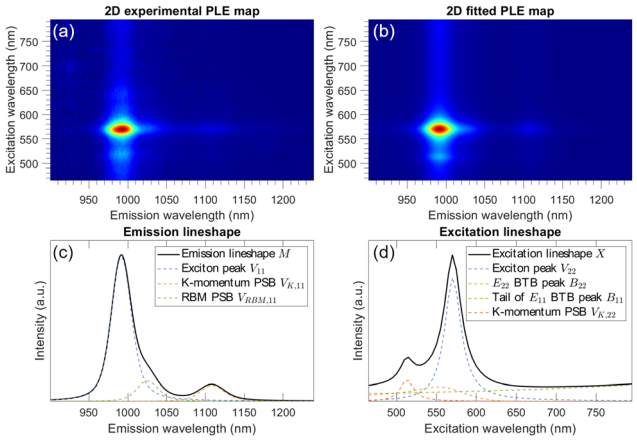

Fig. 1 (a) Experimental PLE map from a (6, 5) sample sorted according to the methods described in ref. 4. (b) Fitted PLE map for this sample. (c) Emission lineshape with each of its components as explained in the text. (d) Excitation lineshape with each of its components as explained in the text.

Hence, to describe the long tails observed in experiments, our model for the excitation lineshape includes not only an excitonic part, but also a BTB contribution. The excitonic part of the main peak in excitation is again modelled by a Voigtian, as was the case in emission:

$$V_{22}(E) := V(E;\, E_{22},\, \sigma_{22},\, \gamma_{22}). \tag{16}$$

For the BTB contribution we assume a simple description and take the lineshape to be proportional to a regularised version of the joint density of states (JDOS) for a quasi-1D system. In particular, a $1/\sqrt{E}$ van Hove singularity is convolved with a Gaussian centered at E_{22} and defined (for simplicity of the model) to have the same FWHM as the excitonic Voigtian (ϕ_{22}):

$$\begin{aligned} B_{22}(E) &:= C(E, E_{22}, \sigma) \\ &= \int_{-\infty}^{\infty} G(E'; E_{22}, \sigma) D(E; E')\mathrm{d}E' \end{aligned} \tag{17}$$

with $\sigma = \dfrac{\phi_{22}}{2\sqrt{2\ln 2}}$ and

$$D(E; E_0) = \frac{\Theta(E - E_0)}{\sqrt{E - E_0}}. \tag{18}$$

Here, $\Theta(x)$ is the Heaviside step function and the result of the integral can be related to the modified Bessel functions $I_\nu(z)$ and $K_\nu(z)$ of order $\nu = \pm\frac{1}{4}$:

$$B_{22}(E) = \begin{cases} \sqrt{\dfrac{-z}{2\pi\sigma_{22}}}\mathrm{e}^{-z^2} K_{\frac{1}{4}}(z^2) & (z < 0) \\ \dfrac{1}{2}\sqrt{\dfrac{\pi z}{\sigma_{22}}}\mathrm{e}^{-z^2}\left[I_{-\frac{1}{4}}(z^2) + I_{\frac{1}{4}}(z^2)\right] & (z \geq 0) \end{cases} \tag{19}$$

where $z = \dfrac{E - E_{22}}{2\sigma_{22}}$.

Thus, the main peak in the excitation lineshape for each chirality consists of the sum

$$V_{22}(E) + A_{\mathrm{BTB},22} B_{22}(E). \tag{20}$$

In theory the amplitudes of the BTB contributions could depend on the nanotube diameter.[17] Such a dependence could be incorporated into our model with a prefactor like that for the

amplitudes of the phonon sidebands. However, none of the samples tested so far have required this and hence we assume $A_{\mathrm{BTB},22}$ to be diameter-independent. For N chiral species this then leads to $3N + 1$ fitting parameters: E_{22}, ϕ_{22}, η_{22} and the chirality-independent amplitude $A_{\mathrm{BTB},22}$.

Due to the long tails in the excitation spectrum, we must include in our model a contribution from excitation at not only E_{22}, but also at E_{11}. Since the E_{11} exciton peak itself lies well outside the excitation range of a typical PLE map, we only need to include the $1/\sqrt{E}$ BTB contribution, without performing the convolution with a Gaussian. We can simply use the unregularised DOS lineshape to model this contribution, since the singularity at E_{11} is far away:

$$B_{11} := D(E; E_{11}). \tag{21}$$

The value of E_{11} is obtained from the emission lineshape $M(E_{\mathrm{em}})$, so this is not a new fit parameter for the full model and this term only adds a single amplitude to the total number of fit parameters, again assumed independent of nanotube chirality.

It is interesting to note that surprisingly good fits are obtained with this excitation profile (see below), even though the use of the standard JDOS is expected to be only an approximation. Indeed, due to Coulomb interactions, the absorption from band-to-band transitions is expected to be proportional not only to this JDOS, but also modulated by the so-called Sommerfeld factors, as first described by Elliott[44] and later further elaborated for 1D systems by Ogawa and Takagahara.[45–47] This effect of Coulomb interactions is expected to flatten the van Hove singularity of the band-to-band transitions near the band edge (transferring oscillator strength to the excitonic transition). That we nevertheless obtain such good fits indicates that this modulation is relatively limited over most of the experimentally studied wavelength range. Indeed, far above the band edge, the excitation profile is expected to approach the classical $1/\sqrt{E}$ dependence asymptotically (Sommerfeld factor converging to 1), and in our fit model, the band-to-band contribution is indeed needed mainly to describe the long tails far from the excitonic transitions. Small deviations near the band edge may remain unnoticeable as they may be absorbed in the fit of the excitonic transition, and in the broadening applied to the band-to-band transition. For the same reason, the small shift between the exciton and the band edge due to the exciton binding energy (which is neglected in our model) may not be noticeable. Moreover, a small change of the relative amplitude of the exciton peak compared to the band-to-band edge is approximately equivalent to such a small shift of the band-to-band edge (as the exciton peak function is similar to the derivative of the band-to-band contribution, which is a step-like function), which may thus be accommodated implicitly in the fits.

Analogous to the emission lineshape, the D-band sideband of the K-momentum dark exciton can be optionally included in the excitation lineshape. As in emission, it is modelled as a Voigtian peak with the same FWHM as the main exciton peak, and its relative position is fitted but again taken to be independent of chirality, adding just one parameter ($E_{\mathrm{K},22}$) to our fit of the excitation spectrum:

$$V_{\mathrm{K},22}(E) := V(E; E_{\mathrm{K},22}, \sigma_{22}, \gamma_{22}). \tag{22}$$

The full model of the excitation spectrum is thus given by

$$X(E_{\mathrm{ex}}) = V_{22}(E_{\mathrm{ex}}) + A_{\mathrm{BTB},22}B_{22}(E_{\mathrm{ex}}) + A_{\mathrm{BTB},11}B_{11}(E_{\mathrm{ex}}) + d^{\beta}A_{\mathrm{K},22}V_{\mathrm{K},22}(E_{\mathrm{ex}}). \tag{23}$$

As explained before, we assume the amplitudes of both BTB contributions to be independent of nanotube chirality and, as in emission, all the amplitudes are measured relative to the main exciton peak. There are hence $3N + 2$ (new) fit parameters in the excitation model, namely E^{i}_{22}, ϕ^{i}_{22} and η^{i}_{22} for each chirality $i := (n, m)$ and two amplitudes $A_{\mathrm{BTB},22}$ and $A_{\mathrm{BTB},11}$. The optional K-momentum PSB adds another two: the amplitude $A_{\mathrm{K},22}$ and the position $E_{\mathrm{K},22} \equiv E^{\mathrm{ex}}_{\mathrm{K},22}$. As previously mentioned, the relative position $E^{\mathrm{ex}}_{\mathrm{K},22}$ of this sideband is fitted in excitation, while the position $E^{\mathrm{em}}_{\mathrm{K},11}$ in emission is directly derived from $E^{\mathrm{ex}}_{\mathrm{K},22}$ and therefore not a fit parameter. We use the same exponent β in the power-law for PSBs in both emission and excitation.

Full 2D map

Combining the models for emission and excitation, we need $3 + 3 + 2 = 8$ parameters (excluding the optional PSBs) to obtain a full fit $F_i(E_{\mathrm{em}}, E_{\mathrm{ex}})$ for a 2D PLE map from a single SWCNT chirality, as detailed above. Since the BTB amplitudes are assumed chirality-independent, analysing a PLE map from a sample of N chiralities then requires $6N + 2$ fit parameters to obtain the individual 2D basis functions F_i while the N amplitudes A_i in (1) are determined by linear regression to weigh the contribution of each chirality to the full map. In case any phonon sidebands are included in the fit, we additionally need chirality-independent amplitudes for each PSB, as well as a (single) exponent β for their diameter dependence. At most this results in an additional 5 fit parameters, irrespective of N.

Finally it is important to note that while the fit is performed in the energy domain, experimental PLE maps are typically measured in the wavelength domain. To this end, experimental data are first internally converted to the energy domain before the fitting procedure, making sure to scale the data appropriately according to the proper Jacobian transformation.[48] After the fit is completed, a conversion back to the wavelength domain is performed for read-out and visualisation.

An example of a fit performed with this model for a multi-chirality HiPco sample, including the K-momentum PSB in excitation, is shown in Fig. 2.

Applications

Our model allows to obtain accurate fits of PLE maps for any SWCNT sample, from which meaningful physical properties such as PL intensities, linewidths, excitation and emission peak positions *etc.* can be extracted. In the following (and in the SI)

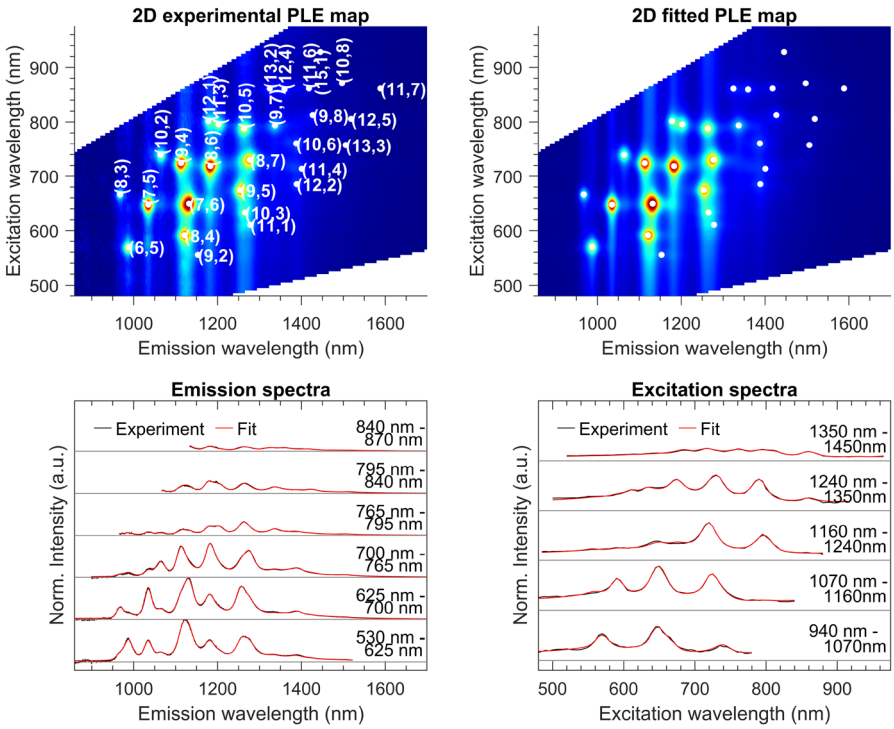

Fig. 2 Illustrative fit for a sample of HiPco SWCNTs. (Top left) Experimental 2D PLE map with chiral indices indicated. (Top right) Fit using our model with fitted peak positions marked as white dots. (Bottom left) Integrated emission spectra (black) and fits (red) for a few excitation intervals. (bottom right) Integrated excitation spectra (black) and fits (red) for a few emission intervals. The fits show very good agreement with the experimental data.

we present a few applications in which this fitting model has been used to extract such physical properties.

SWCNT filling characterisation

The PLE peak positions and linewidths are found to shift and broaden upon filling the SWCNTs with various molecules, in such a way that these shifts and line broadening effects can also be used to evidence the filling of SWCNTs and determine a minimum encapsulation diameter.[14–16] Indeed, this fitting model has been successfully used to evidence the filling of SWCNTs with different dye molecules[14,15,30] as well as to probe the encapsulation of more than 30 different filler molecules with different dielectric constants, finding that the dielectric constant of the filler molecules determines the shift of the SWCNTs' optical transitions.[16] As an example of our model being used for this purpose we show a plot in Fig. 3 from our earlier work on nanotube filling with a dye molecule.[14] The PLE peak positions of dye-filled SWCNTs can be quantitatively compared to those in a reference sample of solvent-filled SWCNTs by computing the shift in the fitted peak position for each chirality. When plotted against nanotube diameter (calculated from n and m after chirality assignment of the observed peaks), this allows one to determine a critical filling diameter for any specific molecule.

Determining the shifts/broadening of the PLE peaks can moreover be important for SWCNTs with different external environments as well.[15] For example, changing the surfactant

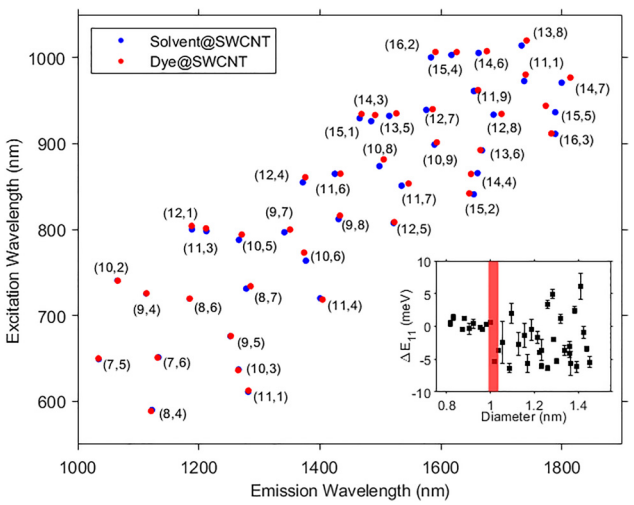

Fig. 3 PLE peak positions for solvent-filled (blue) and dye-filled (red) SWCNTs, as fitted using our model. Inset: Emission peak position shift as a function of tube diameter. The red shaded area provides an estimation of the critical filling diameter for this specific dye molecule. Remade from ref. 14.

structure around SWCNTs clearly results in chirality-dependent shifts of the optical transitions of the SWCNTs, such as those presented in ref. 9 and 10, for which this fitting model could also be highly valuable. Similarly, in situations where shifts or intensity changes of the PL peaks are used as a molecular recognition sensor, an accurate fitting of SWCNT peak

positions, intensities and linewidths could provide a detailed quantitative analysis of the experimental PLE data.[11,49]

Energy transfer from encapsulated dyes or inner SWCNTs in DWCNTs

Previously we have demonstrated the versatility of this fitting model by incorporating also an energy transfer band from an encapsulated dye (1,3-bis[4-(dimethylamino)phenyl]-squaraine) to the SWCNT directly in the excitation profile of our fitting model.[15] This corresponds to absorption by the dye, followed by a transfer of the excitation energy to the SWCNTs which then emit light. The additional component in the excitation profile has its own separate amplitude, linewidth and peak position and its shape was obtained from the absorption spectrum of the dye in solution. Tracking the presence of this component and its position then allowed us to model how the dye's absorption depends on the encapsulating SWCNT's diameter.[15,30] Not only the energy transfer from dyes to surrounding SWCNTs can be probed, but also the highly efficient energy transfer from inner SWCNTs to outer SWCNTs in double-wall CNTs has been fitted in this manner by adapting the model with an additional excitation peak for each inner@outer DWCNT combination.[33]

Chirality-distribution in a sorted SWCNT sample

The intensity of any given peak in a PLE map for a SWCNT sample is related to the abundance of the corresponding chirality in the sample, where the proportionality constant scales with the chirality-dependent fluorescence quantum efficiency of the SWCNTs. Since our model allows to extract these intensities in a quantitatively accurate manner through the linear regression amplitudes $A_{(n,m)}$, we can use this to monitor sample purity in chirality separation efforts.[6,8,31,32] As has been demonstrated earlier,[6,8] the wide range of chiralities typically present in an as-synthesised SWCNT sample can be strongly reduced by applying a sorting method such as aqueous two-phase extraction (ATPE),[5] thus reducing the PL intensity of those chiralities targeted for removal. PLE maps for a few sorted SWCNT samples are shown in Fig. 4 and in SI Fig. S2 obtained *via* ATPE from the multi-chirality HiPco sample for which the PLE map is shown in Fig. 2.

All chiralities that are present in the sorted samples are, by definition, also present in the parent sample. Our model allows us to make use of this fact by including the PLE maps of all three samples in the fitting, and perform the fits simultaneously. Peak positions, linewidths and phonon sideband features are not expected to vary from one sample to another in this set, so we can restrict these to be equal across the data. We find that the BTB contributions however *do* seem to vary between different subsamples. Further investigations are required to determine whether this is an effect of *e.g.* defect density or sample purity, but we can deal with it simply by allowing the BTB contribution amplitudes to vary across the samples. Hence instead of requiring $3 \times (6N + 2)$ fit parameters plus $3 \times N$ linear regression amplitudes we can accurately fit these three maps with $6N + (3 \times 2)$ fit parameters (the same as for one map apart from the number of BTB amplitudes) plus

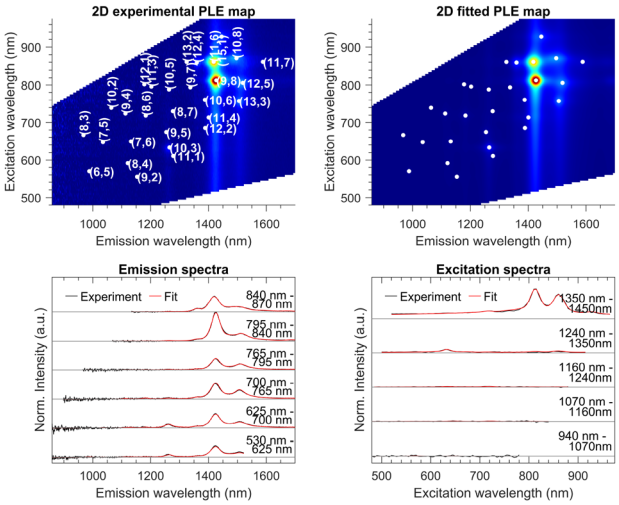

Fig. 4 PLE map and fit for an ATPE separated sample of HiPco SWCNTs with target chirality (9, 8).

$3 \times N$ linear regression amplitudes. Moreover, the fitted values are expected to be more accurate as they are based on more data, especially for chiralities which have a very low abundance in some of the samples.

By doing such a simultaneous fit, we can see chiralities disappear from the sample (when $A_{(n,m)}$ becomes zero), depending on the sorting parameters, as applied in ref. 31 and 32. This allows us to monitor the purity of a sample and visualise it on *e.g.* a hexagonal grid symbolising the graphene sheet from which each chirality is rolled up, as shown in Fig. 5. The effect of the ATPE separation is clearly visible when compared to the parent sample (see Fig. S3 in the SI), but it should be noted that the model amplitudes do not scale to the corresponding chirality abundances directly. The absorption cross-section and PL quantum efficiency vary across different SWCNT chiralities and need to be accounted for in order to transform Fig. 5 from an intensity chart to an abundance distribution. Unfortunately these are currently still largely unknown.[50,51] Examples of such simultaneous fits with the proposed fitting model that

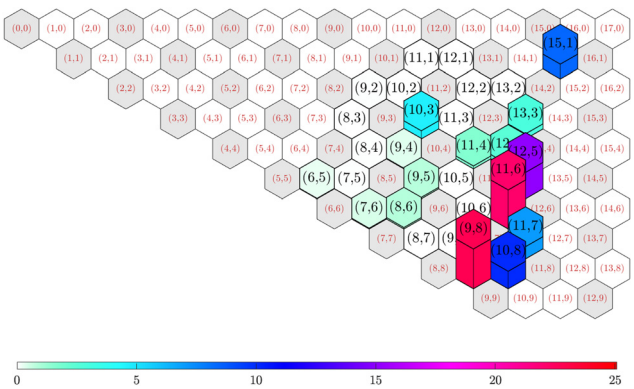

Fig. 5 Summary of PL intensities per chirality as a percentage of the total intensity for the same ATPE separated sample as Fig. 4. Smaller (red) labels denote chiralities that were not taken into account for the fit.

assess the chiral purity of sorted SWCNT samples can be found in ref. 31 and 32.

Fitting empirical relations to the PLE maps

Finally, as presented in eqn (14), the optical transition energies E_{11} and E_{22} can be expressed as a function of diameter and chiral angle in a set of two empirical equations, with 8 different parameters. These parameters will also change when the outer or inner environment of the SWCNT changes. Our fitting model allows to directly fit these empirical relations to the experimental PLE maps, as opposed to the two-step procedure of fitting the full model to the data and subsequently fitting the empirical relations to the fitted peak positions.

In this case the primary objective is not to extract lineshape parameters such as the FWHM, but to obtain good values for the parameters of the empirical relations in certain types of samples. These can then be used for the assignment of chiralities to experimentally observed peaks and as starting values for a more accurate fit with our full model. During such a fit the peak positions are no longer defined by $2N$ fit parameters (E_{11} and E_{22} for all N chiralities in the sample) but rather determined by the empirical relations (14), the 8 parameters of which are fitted instead. All other fit parameters of our model, such as linewidths and PSB features remain present. Such a fitting has successfully been used to extract the empirical relations for many different filler molecules, as presented in ref. 16.

Conclusion

We have developed an accurate fitting model for photoluminescence-excitation spectroscopy data from SWCNTs, by introducing an empirical form for the lineshape in excitation and combining it with the known emission lineshape. The new excitation lineshape consists of two main contributions: an exciton peak (as in emission) modelled as a Voigtian, combined with long tails of background excitation attributed to band-to-band transitions and modeled as a regularised version of the DOS for a quasi-1D system, *i.e.* the convolution of a Gaussian at E_{ii} with $1/\sqrt{E-E_{ii}}$. The long tails mean that this BTB contribution must be included not only from the E_{22} but also from the E_{11} transitions.

The resulting 2D basis function for any given SWCNT chirality is thus determined by only 8 fit parameters: 6 chirality-dependent ones from the positions E_{ii}, linewidths ϕ_{ii} and Voigtian shape parameters η_{ii}. The amplitudes of the BTB contributions relative to the exciton peak make up the other 2. These relative amplitudes, however, are assumed chirality-independent, meaning the full 2D basis functions for N distinct chiral species are fully determined by $6N + 2$ fit parameters. Phonon sidebands in excitation and, if needed, in emission can be included with successively 2 and 3 additional parameters, independent of N, bringing the maximum total number of fit parameters to $6N + 7$.

Herein lies a major strength of our model: by taking full advantage of the optical properties of SWCNTs and making a few reasonable assumptions, we are able to obtain very accurate fits of PLE maps with a surprisingly limited number of fit parameters. Moreover, due to our model's close link with the physical reality, the parameters from a good fit can be meaningfully related to physical quantities such as peak shifts and line broadening due to interaction. The model performs extremely well for a wide range of tested SWCNT samples and has been used to monitor SWCNT sorting using ATPE and to characterise filling of SWCNTs.[6,8,14–16,30–32] Additionally, our model allows for extremely fast simultaneous fitting of multiple samples when positions, linewidths and phonon sideband features are not expected to vary across these samples, such as during ATPE sorting.[6,31,32] Finally, our empirical model for the excitation lineshape allows for fairly straightforward extensions with respect to *e.g.* energy-transfer in PLE for dye-filled SWCNTs[15,30] and from the inner to the outer walls in DWCNTs.[33]

Author contributions

WW wrote the first version of the 2D fit program and derived the excitation lineshape functions of equations (16)–(20). SC added the phonon sidebands to the model and wrote a first version of the GUI. WVW and MDC vastly expanded the GUI with most of its current functionality. ME was responsible for significant validation and optimisation of the GUI code. MM developed much of the error analysis. WW and SC supervised the work. MDC wrote the first draft of the manual for the GUI and all authors contributed to the writing of the final version of the manual. WVW wrote the first draft of the paper and all authors contributed to the writing of the final manuscript.

Conflicts of interest

There are no conflicts to declare.

Data availability

A graphical user interface implementing our 2D PLE fitting model (PLEfit2D) is being distributed under a non-commercial use license at **https://plefit2d.uantwerpen.be**. The version of the software employed for the generation of figures in this work is v1.2.2.

Supplementary information: The fitting implementation, error calculation and convergence tolerance value estimation, as well as additional figures evidencing the versatility of the fitting model. See DOI: **https://doi.org/10.1039/d5nh00231a**.

Acknowledgements

The authors thank Tobias Hertel for useful discussions. SC, MDC, ME, MM and WVW acknowledge funding from the European Research Council Starting Grant No. 679841

(ORDERin1D), MM and WVW acknowledge additional funding from the research fund of the University of Antwerp (BOF DOCPRO4), ME acknowledges financial support by a PhD fellowship from the Research Foundation of Flanders (FWO, grant number: 11C9220N). All authors also acknowledge funding from the Fund for Scientific Research Flanders (FWO, projects G040011N, G021112N, G035918N, G036618N, G0AAM25N and the EOS CHARMING project G0G6218N [EOS-ID 30467715]).

Notes and references

1 S. Reich, C. Thomson and J. Maultzsch, *Carbon nanotubes: Basic Concepts and Physical properties*, Wiley, 2004.
2 H. Kataura, Y. Kumazawa, Y. Maniwa, I. Umezu, S. Suzuki, Y. Ohtsuka and Y. Achiba, *Synth. Met.*, 1999, **103**, 2555–2558.
3 S. M. Bachilo, M. S. Strano, C. Kittrell, R. H. Hauge, R. E. Smalley and R. B. Weisman, *Science*, 2002, **298**, 2361–2366.
4 N. K. Subbaiyan, S. Cambré, A. N. G. Parra-Vasquez, E. H. Hároz, S. K. Doorn and J. G. Duque, *ACS Nano*, 2014, **8**, 1619–1628.
5 J. A. Fagan, *Nanoscale Adv.*, 2019, **1**, 3307–3324.
6 H. Li, G. Gordeev, O. Garrity, N. A. Peyyety, P. B. Selvasundaram, S. Dehm, R. Krupke, S. Cambré, W. Wenseleers, S. Reich, M. Zheng, J. A. Fagan and B. S. Flavel, *ACS Nano*, 2020, **14**, 948–963.
7 F. Yang, M. Wang, D. Zhang, J. Yang, M. Zheng and Y. Li, *Chem. Rev.*, 2020, **120**, 2693–2758.
8 A. Castan, S. Forel, F. Fossard, J. Defillet, A. Ghedjatti, D. Levshov, W. Wenseleers, S. Cambré and A. Loiseau, *Carbon*, 2021, **171**, 968–979.
9 F. F. Bergler, S. Stahl, A. Goy, F. Schöppler and T. Hertel, *Langmuir*, 2016, **32**, 9598–9603.
10 C. M. Sims and J. A. Fagan, *Carbon*, 2020, **165**, 196–203.
11 M. Kim, C. Chen, P. Wang, J. J. Mulvey, Y. Yang, C. Wun, M. Antman-Passig, H.-B. Luo, S. Cho, K. Long-Roche, L. V. Ramanathan, A. Jagota, M. Zheng, Y. Wang and D. A. Heller, *Nat. Biomed. Eng.*, 2022, **6**, 267–275.
12 S. Cambré and W. Wenseleers, *Angew. Chem., Int. Ed.*, 2011, **50**, 2764–2768.
13 S. Cambré, S. M. Santos, W. Wenseleers, A. R. T. Nugraha, R. Saito, L. Cognet and B. Lounis, *ACS Nano*, 2012, **6**, 2649–2655.
14 S. Cambré, J. Campo, C. Beirnaert, C. Verlackt and W. Wenseleers, *Nat. Nanotechnol.*, 2015, **10**, 248–252.
15 S. van Bezouw, D. H. Arias, R. Ihly, S. Cambré, A. J. Ferguson, J. Campo, J. C. Johnson, J. Defillet, W. Wenseleers and J. L. Blackburn, *ACS Nano*, 2018, **12**, 6881–6894.
16 J. Campo, S. Cambré, B. Botka, J. Obrzut, W. Wenseleers and J. A. Fagan, *ACS Nano*, 2021, **15**, 2301–2317.
17 V. Perebeinos, J. Tersoff and P. Avouris, *Phys. Rev. Lett.*, 2005, **94**, 027402.
18 H. Htoon, M. J. O'Connell, S. K. Doorn and V. I. Klimov, *Phys. Rev. Lett.*, 2005, **94**, 127403.
19 S. Chou, F. Plentz, J. Jiang, R. Saito, D. Nezich, H. Ribeiro, A. Jorio, M. Pimenta, G. Samsonidze, A. Santos, M. Zheng, G. Onoa, E. Semke, G. Dresselhaus and M. Dresselhaus, *Phys. Rev. Lett.*, 2005, **94**, 127402.
20 Y. Murakami, B. Lu, S. Kazaoui, N. Minami, T. Okubo and S. Maruyama, *Phys. Rev. B: Condens. Matter Mater. Phys.*, 2009, **79**, 195407.
21 R. Matsunaga, K. Matsuda and Y. Kanemitsu, *Phys. Rev. B: Condens. Matter Mater. Phys.*, 2010, **81**, 033401.
22 X. He, H. Htoon, S. Doorn, W. Pernice, F. Pyatkov, R. Krupke, A. Jeantet, Y. Chassagneux and C. Voisin, *Nat. Mater.*, 2018, **17**, 663–670.
23 J. Zaumseil, *Adv. Opt. Mater.*, 2022, **10**, 2101576.
24 F. Vialla, E. Malic, B. Langlois, Y. Chassagneux, C. Diederichs, E. Deleporte, P. Roussignol, J.-S. Lauret and C. Voisin, *Phys. Rev. B: Condens. Matter Mater. Phys.*, 2014, **90**, 155401.
25 Y. Miyauchi and S. Maruyama, *Phys. Rev. B: Condens. Matter Mater. Phys.*, 2006, **74**, 035415.
26 T. Hertel, V. Perebeinos, J. Crochet, K. Arnold, M. Kappes and P. Avouris, *Nano Lett.*, 2008, **8**, 87–91.
27 F. Vialla, C. Roquelet, B. Langlois, G. Delport, S. M. Santos, E. Deleporte, P. Roussignol, C. Delalande, C. Voisin and J.-S. Lauret, *Phys. Rev. Lett.*, 2013, **111**, 137402.
28 J.-D. R. Rocha, S. M. Bachilo, S. Ghosh, S. Arepalli and R. B. Weisman, *Anal. Chem.*, 2011, **83**, 7431–7437.
29 M. Pfohl, D. D. Tune, A. Graf, J. Zaumseil, R. Krupke and B. S. Flavel, *ACS Omega*, 2017, **2**, 1163–1171.
30 S. Forel, H. Li, S. van Bezouw, J. Campo, L. Wieland, W. Wenseleers, B. S. Flavel and S. Cambré, *Nanoscale*, 2022, **14**, 8385–8397.
31 J. Defillet, M. Avramenko, M. Martinati, M. A. López Carrillo, D. Van der Elst, W. Wenseleers and S. Cambré, *Carbon*, 2022, **195**, 349–363.
32 M. Avramenko, J. Defillet, M. A. López Carrillo, M. Martinati, W. Wenseleers and S. Cambré, *Nanoscale*, 2022, **14**, 15484–15497.
33 M. Erkens, D. Levshov, W. Wenseleers, H. Li, B. S. Flavel, J. A. Fagan, V. N. Popov, M. Avramenko, S. Forel, E. Flahaut and S. Cambré, *ACS Nano*, 2022, **16**, 16038–16053.
34 O. N. Torrens, M. Zheng and J. M. Kikkawa, *Phys. Rev. Lett.*, 2008, **101**, 157401.
35 J. Olivero and R. Longbothum, *J. Quant. Spectrosc. Radiat. Transfer*, 1977, **17**, 233–236.
36 S. G. Johnson, *Faddeeva Package*, 2012, **http://ab-initio.mit.edu/Faddeeva**.
37 P. M. Vora, X. Tu, E. J. Mele, M. Zheng and J. M. Kikkawa, *Phys. Rev. B: Condens. Matter Mater. Phys.*, 2010, **81**, 155123.
38 G. Mahan, *Phys. Rev. B: Condens. Matter Mater. Phys.*, 2002, **65**, 235402.
39 S. Cambré, B. Schoeters, S. Luyckx, E. Goovaerts and W. Wenseleers, *Phys. Rev. Lett.*, 2010, **104**, 207401.
40 M. S. Dresselhaus and P. C. Eklund, *Adv. Phys.*, 2000, **49**, 705–814.
41 M. J. O'Connell, S. M. Bachilo, C. B. Huffman, V. C. Moore, M. S. Strano, E. H. Haroz, K. L. Rialon, P. J. Boul, W. H. Noon,

C. Kittrell, J. Ma, R. H. Hauge, R. B. Weisman and R. E. Smalley, *Science*, 2002, **297**, 593–596.
42 F. Wang, G. Dukovic, L. E. Brus and T. F. Heinz, *Science*, 2005, **308**, 838–841.
43 J. Maultzsch, R. Pomraenke, S. Reich, E. Chang, D. Prezzi, A. Ruini, E. Molinari, M. S. Strano, C. Thomsen and C. Lienau, *Phys. Rev. B: Condens. Matter Mater. Phys.*, 2005, **72**, 241402.
44 R. J. Elliott, *Phys. Rev.*, 1957, **108**, 1384–1389.
45 T. Ogawa and T. Takagahara, *Phys. Rev. B: Condens. Matter Mater. Phys.*, 1991, **43**, 14325–14328.
46 T. Ogawa and T. Takagahara, *Phys. Rev. B: Condens. Matter Mater. Phys.*, 1991, **44**, 8138–8156.
47 H. Haug and S. Koch, *Quantum Theory of the Optical and Electronic Properties of Semiconductors*, World Scientific Publishing, Singapore, 4th edn, 2004.
48 J. Mooney and P. Kambhampati, *J. Phys. Chem. Lett.*, 2013, **4**, 3316–3318.
49 J. Budhathoki-Uprety, J. Shah, J. A. Korsen, A. E. Wayne, T. V. Galassi, J. R. Cohen, J. D. Harvey, P. V. Jena, L. V. Ramanathan, E. A. Jaimes and D. A. Heller, *Nat. Commun.*, 2019, **10**, 3605.
50 D. A. Tsyboulski, J.-D. R. Rocha, S. M. Bachilo, L. Cognet and R. B. Weisman, *Nano Lett.*, 2007, **7**, 3080–3085.
51 X. Wei, T. Tanaka, S. Li, M. Tsuzuki, G. Wang, Z. Yao, L. Li, Y. Yomogida, A. Hirano, H. Liu and H. Kataura, *Nano Lett.*, 2020, **20**, 410–417.